

Towards Graph Neural Network Surrogates Leveraging Mechanistic Expert Knowledge for Pandemic Response

Agatha Schmidt¹,¹ Henrik Zunker¹,¹ Alexander Heinlein²,² Martin J. Kühn^{1,3,*}

¹ Institute of Software Technology, Department of High-Performance Computing,
German Aerospace Center, Cologne, Germany,

² Delft Institute of Applied Mathematics, Delft University of Technology, The Netherlands

³ Life and Medical Sciences Institute, University of Bonn, Bonn, Germany

* Corresponding author; E-mail: martin.kuehn@dlr.de.

Abstract

During the COVID-19 crisis, mechanistic models have been proven fundamental to guide evidence-based decision making. However, time-critical decisions in a dynamically changing environment restrict the time available for modelers to gather supporting evidence. As infectious disease dynamics are often heterogeneous on a spatial or demographic scale, models should be resolved accordingly. In addition, with a large number of potential interventions, all scenarios can barely be computed on time, even when using supercomputing facilities. We suggest to combine complex mechanistic models with data-driven surrogate models to allow for on-the-fly model adaptations by public health experts. We build upon a spatially and demographically resolved infectious disease model and train a graph neural network for data sets representing early phases of the pandemic; cf Fig. 3. The resulting networks reached an execution time of less than a second, a significant speedup compared to the metapopulation approach. The suggested approach yields potential for on-the-fly execution and, thus, integration of disease dynamics models in low-barrier website applications. For the approach to be used with decision-making, datasets with larger variance will have to be considered.

1 Introduction

Mathematical models can help public health experts and decision makers to explore potential future outcomes of ongoing disease dynamics. In particular during the recent COVID-19 cri-

sis, mathematical modeling has been one of the principal forms to provide evidence on the effectiveness of public health and social interventions [1]. With an estimated number of more than 600 000 undiscovered viruses in mammal and avian hosts that are capable of infecting humans [2], pandemic preparedness is compulsory.

Due to local outbreaks and human contact patterns, infectious disease dynamics are often heterogeneous on a spatial or demographic scale. For efficient mitigation of pandemics and accurate predictions, local transmission dynamics should be considered and, if corresponding data is available, this data should be integrated in a mathematical model. Over the last years, a large number of authors has made contributions to predict the development of SARS-CoV-2. Simple ordinary differential equation (ODE)-based SIR (Susceptible-Infected-Removed)-type models [3, 4] have been used for their efficiency in time-critical moments. More flexible integro-differential equation-based models can be used to allow for more realistic disease stage transitions; see, e.g., [5]. Through metapopulation modeling, various authors addressed the spatially heterogeneous spread of SARS-CoV-2 and modeled entire countries with high efficiency [6, 7, 8, 9, 10, 11]. To include individual transmission and superspreading events in an intuitive way, different contact-network-, agent-, or individual-based models have been developed; see, e.g., [12, 13, 14, 15]. However, while more complex models allow to answer more detailed research questions, more complex models generally come at higher computational costs. Recent works [16] combine agent- and equation-based metapopulation approaches to significantly reduce the prediction time of complex agent-based models.

Many models using artificial intelligence (AI) have been proposed to fight the SARS-CoV-2 pandemic. While these models often deliver accurate results in short execution times, a review on more than 650 AI-based models identified most of them to be black box models [17]. Unfortunately, black box models often lack interpretability or explainability and do not contribute to a better understanding of underlying processes. Nevertheless, time is critical factor in pandemics, and evaluations of mitigation and reaction strategies have to be conducted in narrow time windows. In addition, interventions ranging from distancing recommendations to face masks (in particular locations), capacity-restrictions, and closures of venues or even vaccinations (if available) yield a tremendously high combinatorial space from which decision makers need to select. While very simplified models are executed within the range of milliseconds, even highly optimized, complex models might need seconds to minutes to be run. With automated pipelines, preventing manual delay, and high-performance computing [18], thousands or millions of outcomes can be computed on a supercomputing facility to inform decision makers. However, in a dynamically changing environment, decision makers might need expected outcomes for changing initial conditions or other combinations of nonpharmaceutical interventions (NPIs). In addition to NPIs, public recommendations or voluntary behavioral change that can lead to new contact patterns have to be represented in a mathematical model. Eventually, low-barrier access to compute outcomes on all these scenarios through, e.g., a web application, can drastically increase the impact of the developed models.

In this paper, we suggest to combine expert mechanistic modeling with AI-based approaches to work towards an on-the-fly execution of spatially resolved infectious disease models. In [19],

the authors compared advantages and disadvantages of several established machine learning approaches such as random forests, decision trees, and neural networks as surrogates for agent-based models (ABMs). Recently, the authors of [20] employed random forests to calibrate a city-scaled ABM. Here, however, we build upon an already validated spatially and demographically resolved metapopulation model [21] whose predictions we use as data to train a machine learning model. With this model to be executed millions of times on a supercomputing facility overnight, we obtain a good training set a neural network surrogate can generalize from. However, in the present study, we limit ourselves to early outbreak simulation when most of the population is still susceptible. As the output of [21] is already in the form of a graph, a graph-based machine learning model is a natural choice and we therefore propose to employ graph neural networks (GNNs). GNNs are powerful tools for spatially distributed data, which have been introduced in [22] and further popularized in [23]. While we propose GNNs as surrogates for expert mechanistic models of infectious disease dynamics, GNNs have already excelled on data in different applications such as weather predictions [24], Influenza-like diseases [25] or even SARS-CoV-2 [26, 27, 28]. In Fig. 1, we have visualized our approach for a particular autoregressive moving average convolutional (ARMAConv) GNN [29]. After training, the GNN obtains a spatially distributed disease spread (which can be stratified locally according to age groups, sex, or other dimensions) as well as an adjacency matrix for connections between the spatial regions. Upon passing this data through the layers of the trained network, we obtain the predicted disease dynamics, given with the same spatial and demographic resolution. The dynamics will be predicted for up to $n \in \mathbb{N}$ days of prediction and $m = \{c_1, \dots, c_M\}$ contact change points throughout the considered period. Note that the expert model (also denoted as *simulator*) which provides the input data to train the neural network requires the definition of these contact change points m . While $|m| = M$ is arbitrary, it needs to be fixed for a particular model architecture. This means that, if the value of $|m|$ changes, the model has to be retrained, while the same surrogate model can be employed if only the contact change point timings c_1, \dots, c_M vary. We then rely on the generalization properties of the developed model. While the graph would be fully connected and the adjacency matrix dense when considered at a national level (see visualization on the European country scale in [29]), using a more granular NUTS2 or NUTS3 resolution¹ produces a less dense or even sparse adjacency matrix. For instance, the adjacency matrix of [21] for the 400 German counties has only roughly 25 % nontrivial values (approx. 40 000 out of 160 000).

¹<https://ec.europa.eu/eurostat/web/nuts/overview/>

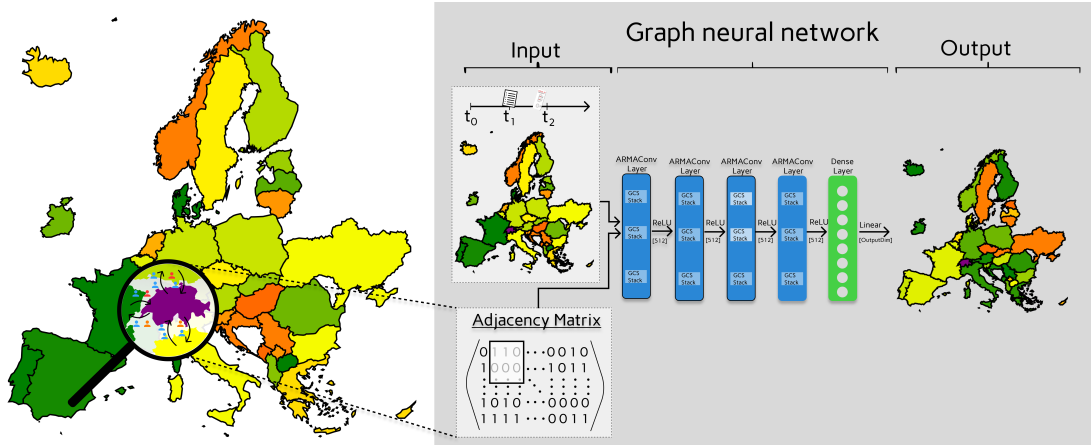


Figure 1: **Visual representation of the prediction phase for a GNN surrogate model.** The adjacency matrix results from the links between the considered regions, here depicted high-level as European countries. The magnifying glass highlights mobility connections between Switzerland and other countries. Colors on the national level geography represent disease outcomes such as symptomatic cases incidence, hospitalization, or deaths. Visualization of a GNN with four ARMAConv layers with three Graph Convolutional Skip (GCS) stacks and one dense output layer. Visualization based on Eurostat shape files [30] © EuroGeographics for the administrative boundaries.

2 Material and Methods

2.1 Mechanistic model

For a trained surrogate model to be reliable, its underlying mechanistic expert model has to integrate the most important disease states and properties of disease dynamics. While deaths are usually monitored, several indicators such as the number of reported cases, the number of hospitalizations or intensive care unit (ICU) admissions have been considered in Germany to implement or lift nonpharmaceutical interventions against SARS-CoV-2 [31]. Consequently, we have chosen an epidemic model based on ODEs that has already been validated in [21] and which classes subpopulations in the infection states *susceptible*, *exposed (not infectious)*, *a- or presymptomatic and infectious*, *mildly symptomatic and infectious*, *severely infected (hospitalized)*, *critically infected (ICU)*, *dead*, and *recovered*; see Fig. 2. Aside the mentioned indicators, the model particularly considers pre- and asymptomatic transmission as studies on SARS-CoV-2 observed that viral load is peaking close to symptom onset [32, 33]. The model is efficiently implemented in C++ in the MEMilio [34] framework, which means that it yields very fast model evaluations on a single core. We furthermore divided the population into $G = 6$ age groups, that is, from 0 to 4, 5 to 14, 15 to 34, 35 to 59, 60 to 79, and 80+ years.

The transmission process is modeled by the susceptible population $S_i(t)$ becoming exposed

($E_i(t)$), through infection of either infectious nonsymptomatic ($I_{NS,i}(t)$) or symptomatic individuals ($I_{Sy,i}(t)$), $i \in \{1, \dots, 6\}$. This can be described by the ODE

$$\frac{dS_i(t)}{dt} = -S_i(t)\rho_i \sum_{j=1}^6 \phi_{i,j}(t) \frac{\xi_{I_{NS},j} I_{NS,j}(t) + \xi_{I_{Sy},j} I_{Sy,j}(t)}{N_j - D_j(t)}, \quad (1)$$

where $\xi_{I_{NS}}$ and $\xi_{I_{Sy}}$ represent the shares of nonisolated a- or presymptomatic and symptomatic infectious individuals, respectively. Furthermore, ρ_i denotes the age-resolved probability of becoming infected from a contact with an infectious person, and $\phi_{i,j}(t)$ represents the mean daily number of contacts between individuals of age group i and age group j . Note $\phi_{i,j}(t)$ only varies in the environment of a contact change point and is otherwise constant; see (2) for details. Additionally, we denote the initial population in age group j by N_j and the number of disease-related deaths in age group j up to time t by $D_j(t)$, $j = 1, \dots, 6$.

The course of disease follows a chain of compartments, where an individual either recovers or moves to an aggravated state. We define $z_{j,i}$ as the j -th disease state for age group i and denote the probability of transition from state $z_{j,i}$ to aggravated state $z_{j+1,i}$ by $\mu_{z_{j,i}}^{z_{j+1,i}}$, while consequently $1 - \mu_{z_{j,i}}^{z_{j+1,i}}$ is the probability of recovery. The average time an individual spends in a given state $z_{j,i}$ is represented by $T_{z_{j,i}}$. For disease states where progression or recovery is possible, i.e., excluding *susceptible*, *exposed (not infectious)*, *recovered*, and *dead*, transition follows the form

$$\frac{dz_{j,i}(t)}{dt} = \frac{\mu_{z_{j-1,i}}^{z_{j,i}}}{T_{z_{j-1,i}}} z_{j-1,i}(t) - \frac{z_{j,i}(t)}{T_{z_{j,i}}},$$

where $z_{j-1,i}$ is the former, less severe state. For the full set of equations, we refer to [21]. In this study, we fixed disease dependent parameters over all age groups; see Table 1.

Contact pattern changes are modeled within the the contact rate matrix $(\phi_{i,j}(t))_{i,j}$. Without loss of generality, let us assume that the first contact change takes place at $c_1 \in \mathbb{R}$ with $c_1 > c_0$, where c_0 is the initial time. For a homogeneous reduction factor $0 \leq r \leq 1$, we define

$$\phi_{i,j}(t) := \begin{cases} \phi_{i,j,0}, & t \leq c_1 \\ \widehat{\phi}_{i,j}(t), & t \in (c_1, c_1 + \delta), \quad 0 < \delta < 1, \\ (1-r)\phi_{i,j,0}, & t \geq c_1 + \delta \end{cases} \quad (2)$$

where, $\phi_{i,j,0}$ is the initial contact rate, δ defines a transition interval, and $\widehat{\phi}_{i,j}$ represents a transition contact rate to ensure smooth transition, i.e., $\phi_{i,j}(t) \in \mathcal{C}^1((t_1 - \epsilon, t_1 + \delta + \epsilon))$ for $i, j \in \{1, \dots, 6\}$ with $0 < \epsilon \ll 1$. In [21] and here, $\widehat{\phi}$ was realized through a cosine function.

In order to realize the spatial resolution, we used a generalized graph as described in [21]. There, each node represented one spatial region with a local disease dynamics model, and we defined one edge for each pair of age groups and disease states to implement mobility exchange. The mobility data was extracted from a combination of data from the German Federal Employment Agency [35] and Twitter. The adjacency matrix needed for the GNN was obtained from

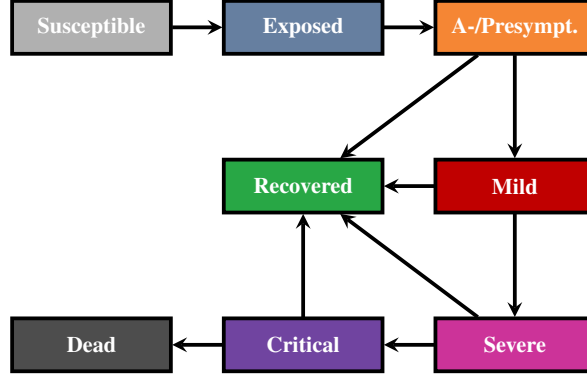


Figure 2: **Disease state transition model.** The disease state transition model comprises eight infection states with possibility for recovery or aggravation after each disease state following exposure state (except for death and recovery itself).

Parameter	Value	Description
T_E	3.2	Duration (in days) in <i>exposed (not infectious)</i> state
T_{INS}	2.0	Duration (in days) in <i>a- or presymptomatic and infectious</i> state
T_{Sy}	6.0	Duration (in days) in <i>mildly symptomatic and infectious</i> state
T_{Sev}	12.0	Duration (in days) in <i>severely infected (hospitalized)</i> state
T_{Cr}	8.0	Duration (in days) in <i>critically infected (ICU)</i> state
ρ	0.1	Transmission risk on contact
ξ_{INS}	0.5	Proportion of not isolated a- or presymptomatic infectious cases
ξ_{Sy}	0.25	Proportion of not isolated symptomatic cases
μ_{INS}^{ISy}	0.91	Proportion of symptomatic cases per all a- and presymptomatic infectious cases
μ_{ISy}^{ISev}	0.2	Proportion of severe cases per symptomatic case
μ_{ISev}^{ICr}	0.25	Proportion of critical cases per severe case
μ_{ICr}^D	0.3	Proportion of deaths per critical case

Table 1: **Model parameters as used for all age groups.**

the mobility matrix by setting all nontrivial values to one. Using the metapopulation approach, we set up an ODE model for each of Germany’s 400 counties. While also the metapopulation model was implemented efficiently and did undergo several optimization steps, for large experiments we still need substantial computing resources. In order to compute a set of initial conditions and spreading patterns for the surrogate model, we varied the initial segmentation into the infection states as well as the number and intensity of contact changes. Each simulation run represented one sample in the data set. The resulting temporal data was split into input days and output days data. In Fig. 3, we provide the box plots for the sampled initializations of the eight compartments for five days prior to the first simulation day. The training data for the GNN contained multiple graphs, each representing a single simulation run. That means that each graph captures the population along all disease states and all region for all output days. In other spatio-temporal graphs [36, 37, 38], each graph represented one moment in time and the goal was to predict the graph and its labels in the next time step.

2.2 Neural network surrogate model

We conducted a multi-stage model building and optimization process to build up a neural network with spatially resolved infection predictions. Before deriving suitable input data structures for learning a spatially resolved graph-based model with a GNN, we considered the temporal evolution of disease dynamics. For this, we trained a Multi-Layer Perceptron (MLP) neural network, a Long Short-Term Memory (LSTM) neural network and a Convolutional Neural Network (CNN), each from the Keras [39] library.

Given the different scales of population-level data in infectious disease dynamics, i.e., the number of susceptibles or recovered is generally several magnitudes larger than the number of hospitalized patients or patients in intensive care, we used a logarithmic scaling of the different disease state trajectories.

For the temporal evolution, we did several substeps. We first considered a population without stratification into age groups. Then, we stratified the population into age groups. For these age groups, we considered age-dependent contact patterns but fixed the disease dependent parameters over all age groups. For all model architectures, we did grid searches on zero to four hidden layers with 32 to 1024 units per layer. Finally, after selecting a suitable neural network architecture, we fine-tuned additional hyperparameters.

After the initial steps, we turned to GNNs. We used the Spektral library [40] for defining the graph data and building the GNNs and Keras to train and evaluate the model. Spektral is an open-source Python library based on Keras API [41] and TensorFlow 2 [42] for the creation of GNNs. Other existing libraries are PyTorchGeometric [43] and DeepGraphLibrary [44].

GNNs can be categorized into spectral and spatial approaches, where spectral approaches have a mathematical foundation in graph signal processing while spatial approaches directly aggregate information from nodes’ spatial neighborhoods [45]. We compared the performance for four model types based on four different layer types available in Spektral. The first network uses GCNConv layers, which are based on the Graph Convolutional Network (GCN) as

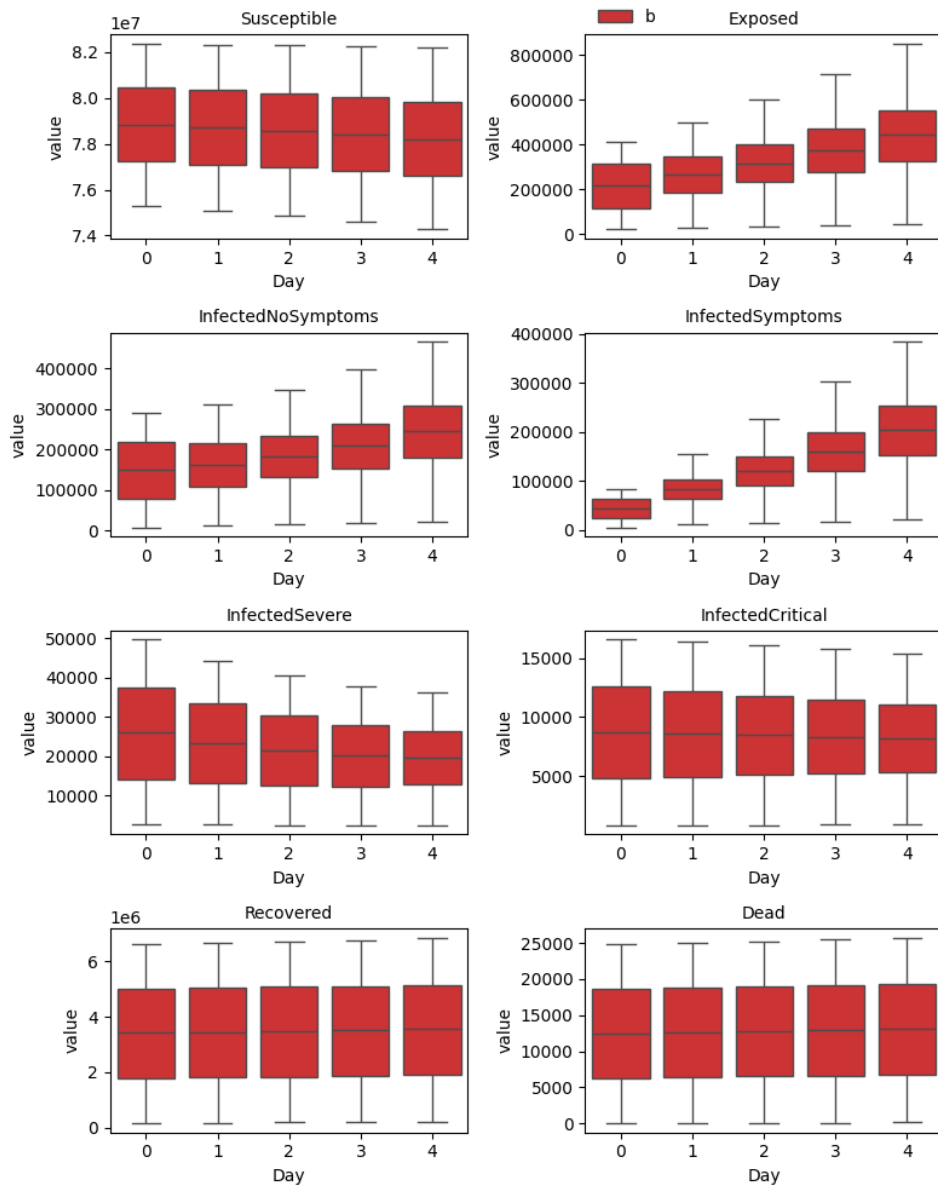


Figure 3: **Sampled variation of initial conditions for the different compartments in the ODE model.**

proposed by [46]. In this spectral approach, a modified adjacency matrix with self-loops is used. The second network uses ARMAConv layers based on [29]. Like the GCNConv layer, this is a spectral approach, and it implements convolutional structures while applying concepts from autoregressive moving average (ARMA) to the learning process. The third network uses Approximative Personalized Propagation of Neural Predictions Convolutional (APPNPConv) layers based on [47], which can also be categorized as a spectral approach with convolutional structures. Lastly and unlike the other networks, the Graph Attention Convolutional (GATConv) layer from [48] is a spatial approach that implements an attention mechanism.

As the ARMAConv layer was selected (see the Results section), we briefly provide some details on the layer type itself and our final architecture. In [29], the authors substituted polynomial filters in GNNs by filters based on the autoregressive moving average. The ARMAConv layer utilizes the technique of autoregressive moving average during the training process using past values and errors in a time series to predict subsequent values.

In our optimized architecture, the ARMAConv layer consists of two parallel stacks of GCS layers, which each serve as a filter on the node feature input data. We thus denote it $ARMA_2$ convolutional layer, and its output is obtained by combining the two parallel stacks of GCS layers; cf. Fig. 1 (right). Both GCS stacks are initialized with random values for the trainable weight matrices \mathbf{W}_2 and \mathbf{V}_2 . This way, it is ensured that each GCS stack outputs a different result at initialization. We conduct two iterations within the CGS stacks, where each iteration corresponds to one graph convolutional layer with a trainable skip connection (CGS layer). One GCS layer corresponds to

$$\bar{\mathbf{X}}_k^{(t+1)} = \sigma(\tilde{\mathbf{A}}\bar{\mathbf{X}}_k^{(t)}\mathbf{W}_k^{(t)} + \bar{\mathbf{X}}^{(0)}\mathbf{V}_k^{(t)}),$$

where σ is an activation function, $\bar{\mathbf{X}}^{(0)}$ are the initial node features, $\bar{\mathbf{X}}^{(t)}$ are filtered node features of the previous iteration, and $\tilde{\mathbf{A}}$ is the normalized adjacency matrix $\tilde{\mathbf{A}} = \mathbf{D}^{-1/2}\mathbf{A}\mathbf{D}^{-1/2}$, which is normalized using the degree matrix \mathbf{D} , which counts for each node the number of adjacent edges, of the graph.

The output of the $ARMA_2$ filter is given by the mean of both GCS stacks

$$\bar{\mathbf{X}} = \frac{1}{2} \sum_{k=1}^2 \bar{\mathbf{X}}_k^{(2)}.$$

3 Results

3.1 Suitable input data structure

In this section, we first provide results on the input data structure for the neural networks to be used. To derive this structure, we have used a multi-stage process, considering components of disease dynamics separately as described before, to iteratively build a complete surrogate model.

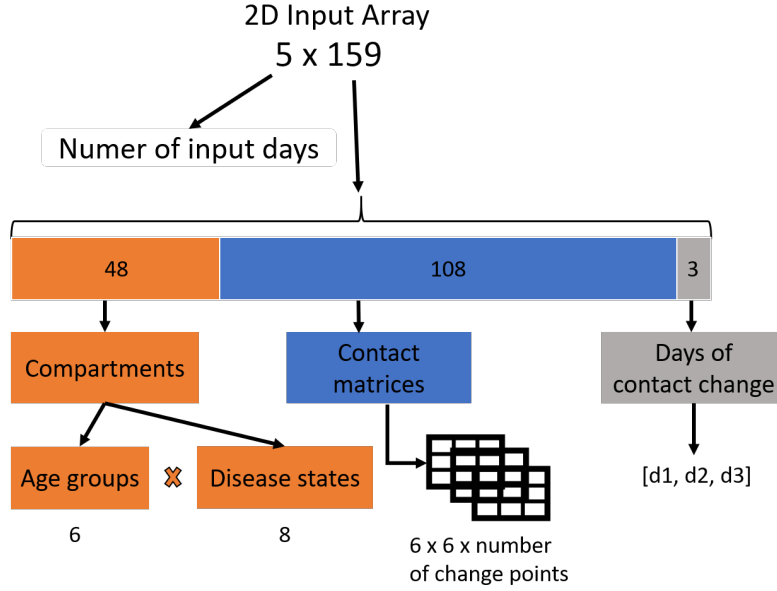


Figure 4: **Simple input data structure.** Data input for simple neural networks (without spatial graph component), divided into age-resolved disease state numbers, contact matrices, and contact change points.

The output of all models is interpolated to full simulation days so that we obtain values for all compartments and potential age groups and regions on a daily base. To evaluate the prediction performance of all neural network-based surrogate models, we consider the mean absolute percentage error (*MAPE*) which is defined as

$$\text{MAPE} := \frac{100}{n} \sum_i \frac{|y_i - \hat{y}_i|}{|y_i|} \quad (3)$$

where n is the number of samples, y_i are the ground truth daily values and \hat{y}_i are the predicted daily values. We use data sets of 10 000 samples for the simple networks and of 1 000 samples for the GNNs.

Under the assumption that no contact change takes place throughout the considered period, it was sufficient to input the temporal trajectories for the different disease states for five days to predict disease dynamics for ongoing 30, 60, 90, 120, or 150 days, consistently showing small test MAPEs (see below). Without contact changes, we thus fed a 2D array with five input days (defining the number of rows) and only 48 compartment values for the six age groups times the eight compartmental values (defining the number of columns); see the orange boxes in Fig. 4. For 30 days prediction horizon, we did a grid search with zero to four hidden layers and 32 to 1024 units per layer to find the best architecture for the simple neural networks. For each grid point, we did a five-fold cross-validation (CV) and computed the *validation MAPE* by the

average over the different MAPEs on the validation sets of the CV splits. Our experiments without stratification in age groups yielded minimum validation MAPEs of 0.20 %, 0.17 %, and 0.13 % for MLP, CNN, and LSTM, respectively. With stratification in six age groups, we obtain minimum validation MAPEs of 0.79 %, 0.80 %, and 0.40 % for MLP, CNN, and LSTM, respectively. After further optimization of the activation function and the optimizer of the LSTM, we applied the best model on a new data set with slightly more variance in the distribution of individuals and obtained test MAPEs below 0.25 % and 0.70 %, without and with age resolution, respectively, and when also considering 60, 90, 120, and 150 days of prediction horizon.

For a more realistic disease dynamics model, we then included contact changes which can be the result of voluntary behavioral change, public recommendations, or nonpharmaceutical interventions. For the surrogate model, the particular reason, due to which contact changes happen, is not important. Given an age-resolved mechanistic expert model with six age groups, any contact change induces a new 6×6 matrix to be used for the ongoing simulation.

Providing the neural networks with information on the contact change, i.e., the new contact matrix as well as the day when the contact change takes place (see the blue boxes in Fig. 4) yielded smaller test MAPEs for MLP and LSTM while the CNN showed significantly larger test MAPEs of 6.6 to 8.2 %. Age-resolved predictions with MLP and LSTM gave test MAPEs of 0.91 % and 0.55 % for one contact change point. Increasing the number of contact change points from 1 to 2, 3, 4, and 5 yielded a maximum test MAPE of 1.47 % for five change points and the LSTM network. With contact change points to be fed, we needed to fix the number of change points over the input (five days) and simulation (30, 60, or more days) period to ensure equally-sized input data. While this seems to be a limitation, an implemented change point does not necessarily mean a (large) change in contact behavior, i.e., a contact reduction factor close to or equal zero, leaves contact patterns (almost) unchanged. Thus, a period with three real change points might also be modeled through a model with four change points where the fourth change point is expected to have minimal to no influence.

Combining the results from our explorational experiments of the simple MLP and LSTM neural networks with some minor adaptations, we defined the input data set structure for the GNNs as shown in Fig. 5 (left). For a GNN to be trained or executed, we had to provide an (additional) adjacency matrix for the considered regions. The adjacency matrix was naturally obtained from the graph-based expert modeling approach. Note that the trained GNN can be applied to adjacency matrices with different structure than those employed in the training phase. While this allows a lot of flexibility, we have not explored the corresponding performance. Furthermore, we flattened the 2D array of Fig. 4 to a 1D array and slightly changed the way contact information is passed. We now pass the contact matrices only once, but additionally pass the contact reduction factors (i.e., the percentage of change with respect to the initial contact pattern). The resulting 1D array then needs to be passed for all regions, i.e., all nodes of the graph. In the example of Fig. 5 (left), we obtained 400 1D arrays of length 354, with 400 equal to the number of graph nodes representing all German counties (NUTS3 level).

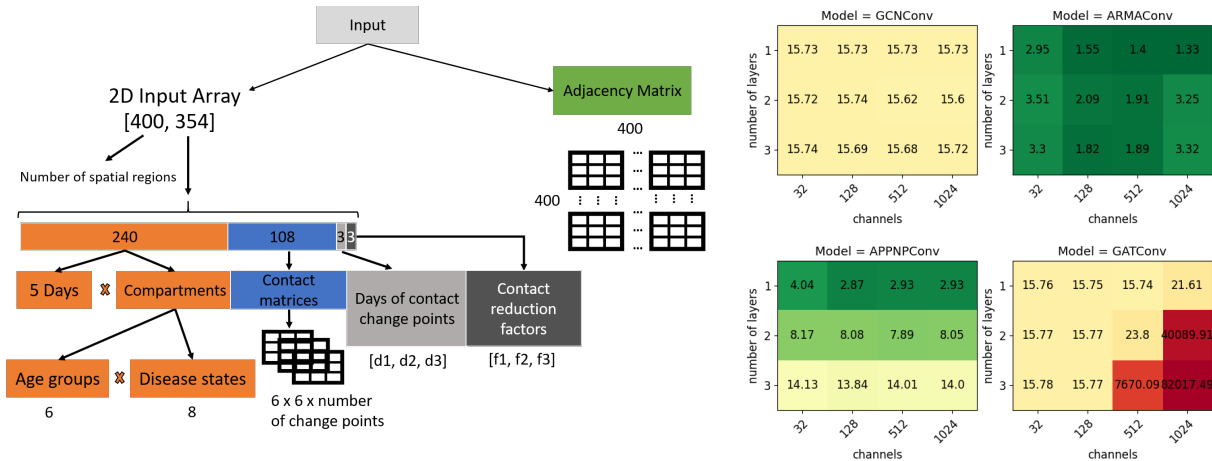


Figure 5: **Input data structure for GNNs (left) and grid search results (right).** *Left:* Input for GNNs consists of initial (five days) disease state values for six age groups, three 6×6 contact matrices, three days of contact change, and three contact reduction factors as well as the adjacency matrix. The dimension of the adjacency matrix is visualized as 400×400 , which comes from the particular application on the 400 German counties. Similarly, the first array dimension of the remaining input is 400. *Right:* Grid search results with 1 to 3 layers and 32 to 1024 channels per layer for GCNConv-, ARMAConv-, APPNPConv-, and GATConv-based architectures, respectively.

3.2 Optimization of the GNN architecture

Having derived a suitable data input structure for a GNN surrogate model, we now had to select an appropriate GNN model and optimize its architecture. We conducted a grid search to identify the model architecture with the best performance, varying the number of layers between one and three and the number of output channels per layer between 32 and 1024. On the grid, we conducted five-fold CV and evaluated the performance of the models by comparing the averaged validation MAPE values from the validation data sets of the CV. As before, we first considered a simplified case without contact changes. While the best architectures for GCNConv and GATConv remain around 15% validation MAPE, APPNPConv’s and ARMAConv’s best architectures attain validation MAPE values of 2.93% and 1.33%, respectively; cf. Fig. 5 (right). We therefore selected an ARMAConv model with one layer and 1024 channels which was, in a next step, optimized by experimenting with model specific parameters provided by the implementation from Spektral; for a brief description of our ARMAConv GNN architecture, we refer to the section Material and Methods. In the optimization and fine-tuning process, we varied the number of GCS stacks (1 and 2), the iterations (1, 2, and 3), and dropout rate (0.0 and 0.2). The best-performing model reached an average validation MAPE of 0.95% on a 30-days prediction horizon. The final model architecture was set to one ARMAConv layer containing two GCS stacks whose filtered response is computed over two iterations.

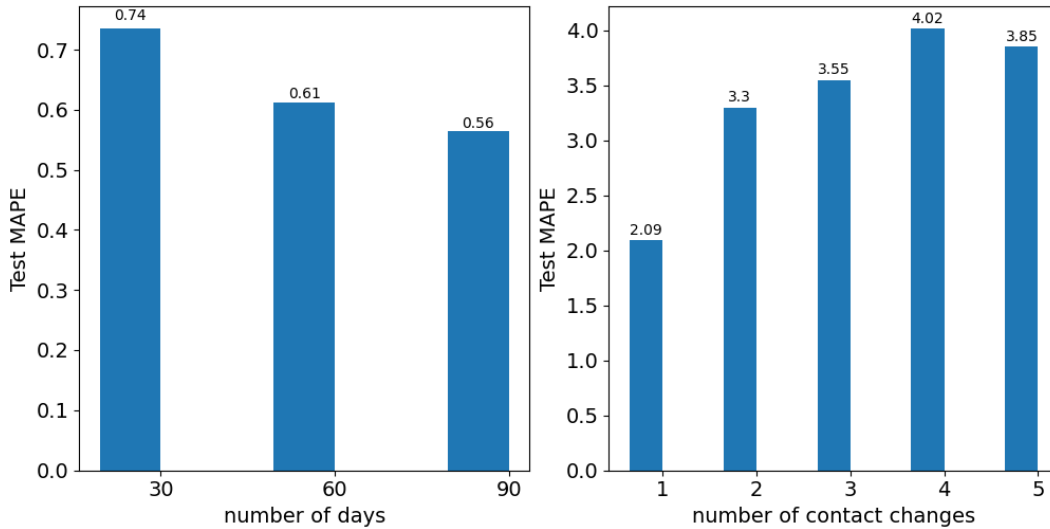


Figure 6: **ARMAConv: Test MAPE for varying prediction horizons (left) and number of contact change points (right).** *Left:* Test MAPEs for prediction horizons of 30, 60, and 90 days. *Right:* Test MAPEs for a prediction horizon of 100 days and one to five contact change points.

Analogously to the simple neural networks employed for predictions without a spatial distribution, we tested the performance of the GNN on tasks with various prediction horizons and numbers of contact change points within a time span of 100 days. As this process is very costly, we used a classic 80-10-10 split in train-validate-test instead of doing a CV. The performance of the model was relatively constant for different prediction horizons. As depicted in Fig. 6 (left), we obtain test MAPEs of 0.74 %, 0.61 %, and 0.56 % on 30, 60, and 90 prediction days, respectively. By implementing up to five contact change points into the model, we obtain test MAPEs with values ranging from 2.09 % to 3.85 %; see Fig. 6.

3.3 Execution Time Performance

In the previous section, we developed a GNN surrogate model that yielded test MAPEs between 2.09 % and 3.85 % percent, when predicting spatially and demographically resolved disease dynamics over the 400 counties of Germany. In this section, we show how the surrogate model outperforms the expert mechanistic model in terms of execution times. Timings were measured on a GPU-accelerated Intel Xeon Scalable Processor "Skylake" Silver node with four NVIDIA Tesla V100 SXM2 16 GB.

To support a just-in-time, e.g., web-based, exploration of different scenarios by manually adapting one parameter at a time requires one single model prediction for every parameter change. When predefining multiple scenarios in a joint space over different parameters, e.g., the implementation of interventions to be evaluated on different days (e.g., today, in three days, and

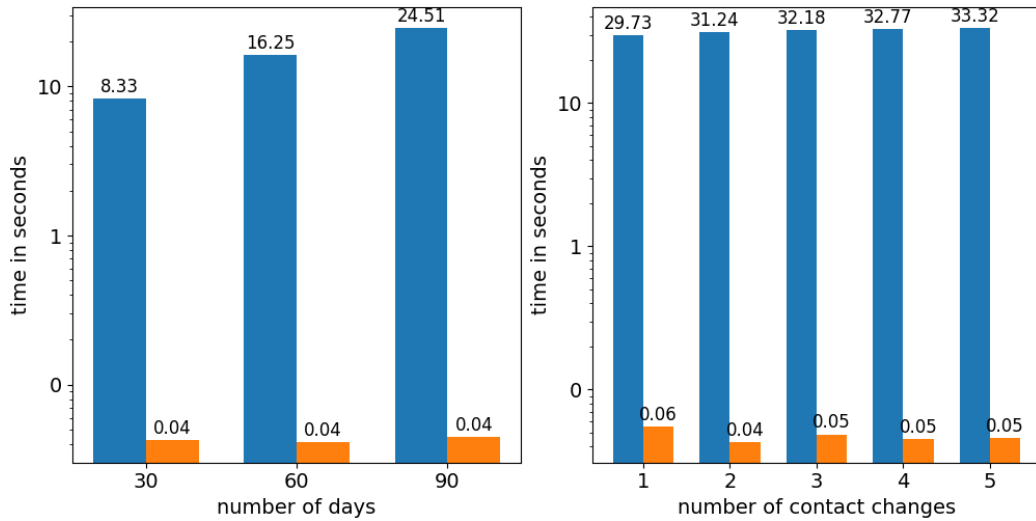
in one week) and with varying strictness (e.g., restricting gatherings to 10, 20, or 50 persons), a batch of multiple predictions are needed. With a factor space in just two or three dimensions and two or three discrete values, we need between four and 27 model predictions. In Fig. 7, we thus provide measured run times for one and 10 executions of the expert and the surrogate model, respectively. Firstly, we observed that the expert model runtime scales, as expected, linearly with the prediction horizon while the GNN surrogate model provided results in (almost) constant time, independent of the horizon. Furthermore, the execution time of the expert model scaled linearly with the number of executions (without parallelization) while the scaling of the GNN surrogate model was clearly superior: for instance, the time was only doubled to tripled from one to ten model executions. Both models showed run times independent on the number of contact change points. Overall, the neural network sped up the prediction process by 537 to 726 times for a single model execution and by 2171 to 2423 times for for ten model executions. With approximately 0.05 seconds for one sample and 0.13 seconds for 10 samples, the surrogate model can be employed on-the-fly.

4 Discussion

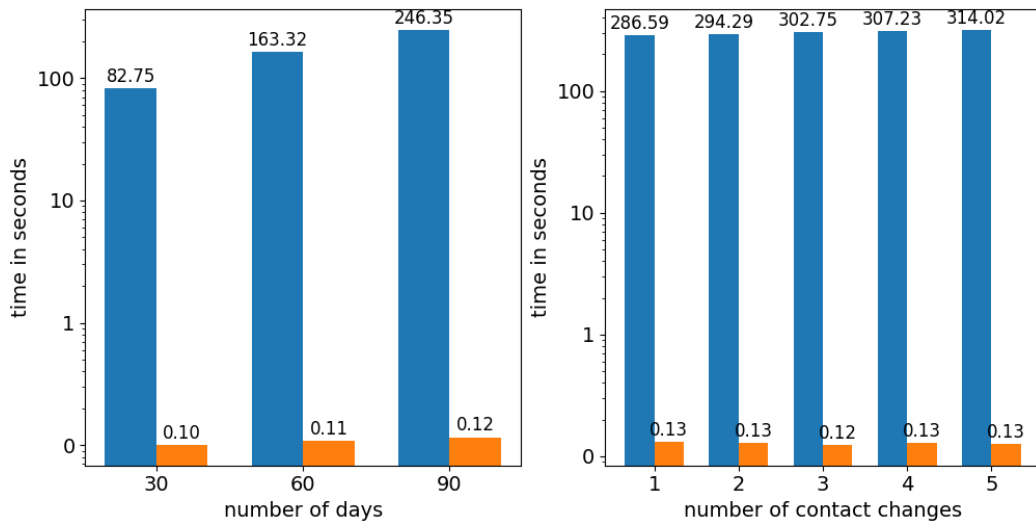
Surrogate models are a cost-efficient technique to approximate the behavior of complex models. Usually, the more complex the reference model is, the higher the requirement of computational resources. The goal of the surrogate model is to approximate the original model’s behavior more efficiently while achieving accuracies close to the original model. In time-critical epidemic or pandemic situations, the evaluation of a large set of potential reactions is recommended, and swift reaction is crucial. Unfortunately, supercomputing resources might not be available on-the-fly or predictions are needed by stakeholders which do not have access to supercomputing facilities. To overcome these barriers and to provide just-in-time answers to urgent questions, (pre)trained surrogate models can become of great aid for decision makers and substantially increase the impact of mathematical-epidemiological modeling.

In this article, we presented a surrogate model based on neural networks that is capable of handling spatial resolution. While several recent surrogate models are based on the concept of physics-informed neural networks [49, 50, 51], our surrogate model is entirely data-driven and uses a “physics”-based a simulator only to create reliable training data. On the one hand, this means that physical constraints such as population conservation are not considered explicitly. On the other hand, our approach offers a significant advantage, as particular modifications to the original model do not require changes in the surrogate model; only new training data has to be generated and the model has to be retrained. We have not yet investigated if our surrogate model could further benefit from integrating “physical” constraints such as population conservation into the loss function; however, this is out of the scope of this paper.

Although we used age-resolved mechanistic and GNN models, we fixed the disease parameters over all groups and contact reductions in this study were applied homogeneously to all age groups. As NPIs such as school closures or remote work policies often target particular age



a) Prediction of a single sample.



b) Prediction of 10 samples.

Figure 7: **Runtime comparison between GNN surrogate model and expert mechanistic model of [21]**. The execution times of the expert mechanistic model are shown by blue bars and the execution times of the developed GNN surrogate model (ARMAConV) are shown by orange bars. The plots on the left hand side show the measured timings over a prediction horizon of 30, 60, and 90 days, respectively. The plots on the right hand side show the measured timings over a 100-days prediction horizon with different numbers of contact change points. In the upper row [a)], we present the timings for one single sample or realization of the model and in the bottom row [b)], we present results for 10 different realizations.

groups, heterogeneous settings should be studied in future research. While an implementation of heterogeneously changing contact patterns would be straightforward, we have not investigated how this would affect the performance of the surrogate model. Similarly, we did not consider spatially heterogeneous interventions, which will be considered in future research. In both cases, when increasing the complexity of the contact restrictions, we expect that a larger data set would be required to obtain a similar model performance.

A large limitation of the study in its current form is the relatively little variance in the initially infected population (cf. Fig. 3) and the fact that we do not consider reinfection (cf. Fig. 2). This means that the model in its current form has not been validated for later stage epidemic situations or more input settings.

In this study, we first compared four different types of GNN layers which all build on the binary adjacency matrix to incorporate spatial resolution and exchange. Although our model architecture already provides convincing results, none of the considered approaches took the highly varying values for traveling and commuting activities between the different spatial regions into account. We expect that our model could be further improved when utilizing these edge weights in the training process. Promising directions to develop a surrogate model with edge weights are given by the CrystalConv [52] or XENetConv [53] layer. Unfortunately, on a single NVIDIA Quadro RTX 6000, the memory were not sufficient to train a graph with 40 000 edges.

Eventually, this study shed light on the performance of a GNN surrogate model using the same graph connectivity in training and evaluation processes. In this, we did not explore the generalization potential of the GNN surrogate model to other graphs than the one used for training. The corresponding outcome will be even more interesting when layers with edge weights as given above will be used.

With certain limitations and directions for future work, we presented a surrogate model using methods of artificial intelligence that naturally integrate spatial distributions. The presented GNN performed well on the yet to be extended data sets for disease dynamics and nonpharmaceutical interventions on all 400 counties of Germany. It was able to make predictions with small MAPEs over time horizons between 30 and 150 days (simple NNs, not accounting for spatial effects) and 100 (GNNs, incorporating the spatial distribution) days, respectively, integrating contact pattern changes of the population at up to five days during the considered period. Our surrogate model delivered spatially and demographically resolved disease dynamics for a prediction horizon of several months and sped up the prediction process significantly. As these results could be computed within a fraction of a second, our model is capable of being integrated in web-based application.

Acknowledgements

AS thanks Simon Vollendorf for exchange on neural network models and technical considerations to run them. This work was supported by the Initiative and Networking Fund of the

Helmholtz Association (grant agreement number KA1-Co-08, Project LOKI-Pandemics) and by the German Federal Ministry for Digital and Transport under grant agreement FKZ19F2211A (Project PANDEMOS).

References

- [1] European Centre for Disease Prevention and Control, Public health and social measures for health emergencies and pandemics in the EU/EEA: recommendations for strengthening preparedness planning, Tech. rep. (2024). doi:10.2900/253991.
- [2] P. Daszak, J. Amuasi, C. das Neves, D. Hayman, T. Kuiken, B. Roche, C. Zambrana-Torrel, P. Buss, H. Dunderova, Y. Feferholtz, G. Foldvari, E. Igbinosa, S. Junglen, Q. Liu, G. Suzan, M. Uhart, C. Wannous, K. Woolaston, P. Mosig Reidl, K. O'Brien, U. Pascual, P. Stoett, H. Li, H. T. Ngo, Workshop Report on Biodiversity and Pandemics of the Intergovernmental Platform on Biodiversity and Ecosystem Services (IPBES), Tech. rep. (Oct. 2020).
URL <https://doi.org/10.5281/zenodo.7432079>
- [3] S. Bauer, S. Contreras, J. Dehning, M. Linden, E. Iftekhar, S. B. Mohr, A. Olivera-Nappa, V. Priesemann, Relaxing restrictions at the pace of vaccination increases freedom and guards against further COVID-19 waves, PLoS computational biology 17 (9) (2021) e1009288, publisher: Public Library of Science San Francisco, CA USA.
- [4] L. Schüler, J. M. Calabrese, S. Attinger, Data driven high resolution modeling and spatial analyses of the COVID-19 pandemic in Germany, PLOS ONE 16 (8) (2021) e0254660. doi:10.1371/journal.pone.0254660.
- [5] A. C. Wendler, L. Plötzke, H. Tritzschak, M. J. Kühn, A nonstandard numerical scheme for a novel secir integro differential equation-based model with nonexponentially distributed stay times. Submitted for publication. (2024).
URL <https://arxiv.org/abs/2408.12228>
- [6] S. Pei, S. Kandula, J. Shaman, Differential effects of intervention timing on COVID-19 spread in the United States, Science Advances 6 (49) (2020) eabd6370. doi:10.1126/sciadv.abd6370.
- [7] X. Chen, A. Zhang, H. Wang, A. Gallaher, X. Zhu, Compliance and containment in social distancing: mathematical modeling of COVID-19 across townships, International Journal of Geographical Information Science 35 (3) (2021) 446–465, publisher: Taylor & Francis
eprint: <https://doi.org/10.1080/13658816.2021.1873999>. doi:10.1080/13658816.2021.1873999.

- [8] M. W. Levin, M. Shang, R. Stern, Effects of short-term travel on COVID-19 spread: A novel SEIR model and case study in Minnesota, *PLOS ONE* 16 (1) (2021) e0245919, publisher: Public Library of Science. doi:10.1371/journal.pone.0245919.
- [9] J. Liu, G. P. Ong, V. J. Pang, Modelling effectiveness of COVID-19 pandemic control policies using an Area-based SEIR model with consideration of infection during interzonal travel, *Transportation Research Part A: Policy and Practice* 161 (2022) 25–47. doi:10.1016/j.tra.2022.05.003.
- [10] W. Koslow, M. J. Kühn, S. Binder, M. Klitz, D. Abele, A. Basermann, M. Meyer-Hermann, Appropriate relaxation of non-pharmaceutical interventions minimizes the risk of a resurgence in SARS-CoV-2 infections in spite of the Delta variant, *PLOS Computational Biology* 18 (5) (2022) e1010054. doi:10.1371/journal.pcbi.1010054.
- [11] H. Zunker, R. Schmieding, D. Kerkmann, A. Schengen, S. Diexer, R. Mikolajczyk, M. Meyer-Hermann, M. J. Kühn, Novel travel time aware metapopulation models: A combination with multi-layer waning immunity to assess late-phase epidemic and endemic scenarios (Mar. 2024). doi:10.1101/2024.03.01.24303602.
- [12] A. Bershteyn, J. Gerardin, D. Bridenbecker, C. W. Lorton, J. Bloedow, R. S. Baker, G. Chabot-Couture, Y. Chen, T. Fischle, K. Frey, J. S. Gauld, H. Hu, A. S. Izzo, D. J. Klein, D. Lukacevic, K. A. McCarthy, J. C. Miller, A. L. Ouedraogo, T. A. Perkins, J. Steinkraus, Q. A. ten Bosch, H.-F. Ting, S. Titova, B. G. Wagner, P. A. Welkhoff, E. A. Wenger, C. N. Wiswell, for the Institute for Disease Modeling, Implementation and applications of EMOD, an individual-based multi-disease modeling platform, *Pathogens and Disease* 76 (5) (Jul. 2018). doi:10.1093/femspd/fty059.
- [13] C. C. Kerr, R. M. Stuart, D. Mistry, R. G. Abeysuriya, K. Rosenfeld, G. R. Hart, R. C. Núñez, J. A. Cohen, P. Selvaraj, B. Hagedorn, L. George, M. Jastrzebski, A. S. Izzo, G. Fowler, A. Palmer, D. Delpont, N. Scott, S. L. Kelly, C. S. Bennette, B. G. Wagner, S. T. Chang, A. P. Oron, E. A. Wenger, J. Panovska-Griffiths, M. Famulare, D. J. Klein, Covasim: An agent-based model of COVID-19 dynamics and interventions, *PLOS Computational Biology* 17 (7) (2021) 1–32, publisher: Public Library of Science. doi:10.1371/journal.pcbi.1009149.
- [14] S. A. Müller, M. Balmer, W. Charlton, R. Ewert, A. Neumann, C. Rakow, T. Schlenther, K. Nagel, Predicting the effects of COVID-19 related interventions in urban settings by combining activity-based modelling, agent-based simulation, and mobile phone data, *medRxiv* (2021). doi:10.1101/2021.02.27.21252583.
- [15] D. Kerkmann, S. Korf, K. Nguyen, D. Abele, A. Schengen, C. Gerstein, J. H. Göbbert, A. Basermann, M. J. Kühn, M. Meyer-Hermann, Agent-based modeling for realistic reproduction of human mobility and contact behavior to evaluate test and isolation strategies in epidemic infectious disease spread (2024). arXiv:2410.08050.

- [16] J. Bicker, R. Schmieding, M. Meyer-Hermann, M. J. Kühn, Hybrid metapopulation agent-based epidemiological models for efficient insight on the individual scale: a contribution to green computing (2024).
- [17] M.-H. Tayarani N., Applications of artificial intelligence in battling against covid-19: A literature review, *Chaos, Solitons, and Fractals* 142 (2021) 110338. doi:10.1016/j.chaos.2020.110338.
- [18] S. Memon, J. F. Jadebeck, M. Osthege, A. Wendler, D. Kerkmann, H. Zunker, W. Wiechert, K. Nöh, J. H. Göbbert, B. Hagemeyer, M. Riedel, M. J. Kühn, Automated Processing of Pipelines Managing Now- and Forecasting of Infectious Diseases, in: 2024 47th MIPRO ICT and Electronics Convention (MIPRO), IEEE, Opatija, Croatia, 2024, pp. 1157–1162. doi:10.1109/MIPRO60963.2024.10569336.
- [19] C. Angione, E. Silverman, E. Yaneske, Using machine learning as a surrogate model for agent-based simulations, *PloS One* 17 (2) (2022) e0263150. doi:10.1371/journal.pone.0263150.
- [20] C. Robertson, C. Safta, N. Collier, J. Ozik, J. Ray, Bayesian calibration of stochastic agent based model via random forest, arXiv:2406.19524 [cs, stat] (Jun. 2024). URL <http://arxiv.org/abs/2406.19524>
- [21] M. J. Kühn, D. Abele, T. Mitra, W. Koslow, M. Abedi, K. Rack, M. Siggel, S. Khailaie, M. Klitz, S. Binder, L. Spataro, J. Gilg, J. Kleinert, M. Häberle, L. Plötzke, C. D. Spinner, M. Stecher, X. X. Zhu, A. Basermann, M. Meyer-Hermann, Assessment of effective mitigation and prediction of the spread of SARS-CoV-2 in Germany using demographic information and spatial resolution, *Mathematical Biosciences* (2021) 108648 doi:https://doi.org/10.1016/j.mbs.2021.108648.
- [22] M. Gori, G. Monfardini, F. Scarselli, A new model for learning in graph domains, in: *Proceedings. 2005 IEEE International Joint Conference on Neural Networks, 2005.*, Vol. 2, 2005, pp. 729–734 vol. 2, iSSN: 2161-4407. doi:10.1109/IJCNN.2005.1555942.
- [23] F. Scarselli, M. Gori, A. C. Tsoi, M. Hagenbuchner, G. Monfardini, The Graph Neural Network Model, *IEEE Transactions on Neural Networks* 20 (1) (2009) 61–80, conference Name: *IEEE Transactions on Neural Networks*. doi:10.1109/TNN.2008.2005605.
- [24] R. Lam, A. Sanchez-Gonzalez, M. Willson, P. Wirnsberger, M. Fortunato, F. Alet, S. Ravuri, T. Ewalds, Z. Eaton-Rosen, W. Hu, A. Merose, S. Hoyer, G. Holland, O. Vinyals, J. Stott, A. Pritzel, S. Mohamed, P. Battaglia, Learning skillful medium-range global weather forecasting, *Science* 382 (6677) (2023) 1416–1421. doi:10.1126/science.adi2336.

- [25] S. Deng, S. Wang, H. Rangwala, L. Wang, Y. Ning, Graph Message Passing with Cross-location Attentions for Long-term ILI Prediction, 2019.
- [26] A. Kapoor, X. Ben, L. Liu, B. Perozzi, M. Barnes, M. Blais, S. O’Banion, Examining COVID-19 Forecasting using Spatio-Temporal Graph Neural Networks, 2020.
- [27] J. Gao, R. Sharma, C. Qian, L. M. Glass, J. Spaeder, J. Romberg, J. Sun, C. Xiao, STAN: spatio-temporal attention network for pandemic prediction using real-world evidence, *Journal of the American Medical Informatics Association* 28 (4) (2021) 733–743. doi:10.1093/jamia/ocaa322.
- [28] G. Panagopoulos, G. Nikolentzos, M. Vazirgiannis, Transfer Graph Neural Networks for Pandemic Forecasting, *Proceedings of the AAAI Conference on Artificial Intelligence* 35 (6) (2021) 4838–4845, number: 6. doi:10.1609/aaai.v35i6.16616.
- [29] F. M. Bianchi, D. Grattarola, L. Livi, C. Alippi, Graph Neural Networks with Convolutional ARMA Filters, *IEEE Transactions on Pattern Analysis and Machine Intelligence* PP (2021) 1–1. doi:10.1109/TPAMI.2021.3054830.
- [30] Eurostat, Nuts 2024, <https://ec.europa.eu/eurostat/de/web/gisco/geodata/statistical-units/territorial-units-statistic>, accessed: 2024-10-10.
URL <https://ec.europa.eu/eurostat/de/web/gisco/geodata/statistical-units/territorial-units-statistic>
- [31] Robert Koch Institute (RKI), ControlCOVID: Strategie und Handreichung zur Entwicklung von Stufenkonzepten bis Frühjahr 2021, Tech. rep., Robert Koch Institute, Stand 19.03.2021, Änderung: Grenzwerte des Indikators Hospitalisierungsinzidenz (2021).
URL https://www.rki.de/DE/Content/InfAZ/N/Neuartiges_Coronavirus/Downloads/Stufenplan-Fruuehjahr21.pdf?__blob=publicationFile
- [32] K. A. Walsh, S. Spillane, L. Comber, K. Cardwell, P. Harrington, J. Connell, C. Teljeur, N. Broderick, C. F. De Gascun, S. M. Smith, M. Ryan, M. O’Neill, The duration of infectiousness of individuals infected with SARS-CoV-2, *Journal of Infection* 81 (6) (2020) 847–856. doi:10.1016/j.jinf.2020.10.009.
- [33] O. Puhach, B. Meyer, I. Eckerle, SARS-CoV-2 viral load and shedding kinetics, *Nature Reviews Microbiology* 21 (3) (2023) 147–161, publisher: Nature Publishing Group. doi: 10.1038/s41579-022-00822-w.
- [34] M. J. Kühn, D. Abele, D. Kerkmann, S. A. Korf, H. Zunker, A. C. Wendler, J. Bicker, D. K. Nguyen, R. Schmieding, L. Plötzke, P. Lenz, M. F. Betz, C. Gerstein, A. Schmidt, P. Johannssen, M. Klitz, S. Binder, M. Siggel, W. Koslow, J. Kleinert, K. Rack, A. Lutz,

- M. Meyer-Hermann, MEMilio v1.0.0 - A high performance Modular Epidemics simulation software (Dec. 2023).
URL <https://elib.dlr.de/201660/>
- [35] Bundesagentur für Arbeit, Pendlerverflechtungen der sozialversicherungspflichtig Beschäftigten nach Kreisen - Deutschland (Jahreszahlen) (2020).
URL https://statistik.arbeitsagentur.de/SiteGlobals/Forms/Suche/Einzelheftsuche_Formular.html?nn=24390&topic_f=beschaeftigung-pendler-krpend
- [36] Y. Li, R. Yu, C. Shahabi, Y. Liu, Diffusion Convolutional Recurrent Neural Network: Data-Driven Traffic Forecasting, arXiv:1707.01926 [cs, stat] (Feb. 2018). doi:10.48550/arXiv.1707.01926.
- [37] S. Yan, Y. Xiong, D. Lin, Spatial Temporal Graph Convolutional Networks for Skeleton-Based Action Recognition, Proceedings of the AAAI Conference on Artificial Intelligence 32 (1) (Apr. 2018). doi:10.1609/aaai.v32i1.12328.
- [38] B. Yu, H. Yin, Z. Zhu, Spatio-Temporal Graph Convolutional Networks: A Deep Learning Framework for Traffic Forecasting, in: Proceedings of the Twenty-Seventh International Joint Conference on Artificial Intelligence, International Joint Conferences on Artificial Intelligence Organization, Stockholm, Sweden, 2018, pp. 3634–3640. doi:10.24963/ijcai.2018/505.
- [39] F. Chollet, et al., Keras (2015).
URL <https://keras.io>
- [40] D. Grattarola, C. Alippi, Graph Neural Networks in TensorFlow and Keras with Spectral [Application Notes], IEEE Computational Intelligence Magazine 16 (2021) 99–106. doi:10.1109/MCI.2020.3039072.
- [41] F. Chollet, et al., Keras, <https://keras.io> (2015).
- [42] M. Abadi, A. Agarwal, P. Barham, E. Brevdo, Z. Chen, C. Citro, G. S. Corrado, A. Davis, J. Dean, M. Devin, S. Ghemawat, I. Goodfellow, A. Harp, G. Irving, M. Isard, Y. Jia, R. Jozefowicz, L. Kaiser, M. Kudlur, J. Levenberg, D. Mané, R. Monga, S. Moore, D. Murray, C. Olah, M. Schuster, J. Shlens, B. Steiner, I. Sutskever, K. Talwar, P. Tucker, V. Vanhoucke, V. Vasudevan, F. Viégas, O. Vinyals, P. Warden, M. Wattenberg, M. Wicke, Y. Yu, X. Zheng, TensorFlow: Large-scale machine learning on heterogeneous systems, software available from tensorflow.org (2015).
URL <https://www.tensorflow.org/>
- [43] M. Fey, J. E. Lenssen, Fast Graph Representation Learning with PyTorch Geometric, original-date: 2017-10-06T16:03:03Z (May 2019).
URL https://github.com/pyg-team/pytorch_geometric

- [44] M. Wang, D. Zheng, Z. Ye, Q. Gan, M. Li, X. Song, J. Zhou, C. Ma, L. Yu, Y. Gai, T. Xiao, T. He, G. Karypis, J. Li, Z. Zhang, Deep Graph Library: A Graph-Centric, Highly-Performant Package for Graph Neural Networks, arXiv:1909.01315 [cs, stat] (Aug. 2020). doi:10.48550/arXiv.1909.01315.
- [45] Z. Wu, S. Pan, F. Chen, G. Long, C. Zhang, P. S. Yu, A Comprehensive Survey on Graph Neural Networks, IEEE Transactions on Neural Networks and Learning Systems 32 (1) (2021) 4–24. doi:10.1109/TNNLS.2020.2978386.
- [46] T. N. Kipf, M. Welling, Semi-Supervised Classification with Graph Convolutional Networks, arXiv:1609.02907 [cs, stat] (Feb. 2017). doi:10.48550/arXiv.1609.02907.
- [47] J. Gasteiger, A. Bojchevski, S. Günnemann, Predict then Propagate: Graph Neural Networks meet Personalized PageRank, arXiv:1810.05997 [cs, stat] (Apr. 2022). doi:10.48550/arXiv.1810.05997.
- [48] P. Veličković, G. Cucurull, A. Casanova, A. Romero, P. Liò, Y. Bengio, Graph Attention Networks, arXiv:1710.10903 [cs, stat] (Feb. 2018). doi:10.48550/arXiv.1710.10903.
- [49] G. Calzolari, W. Liu, Deep learning to replace, improve, or aid CFD analysis in built environment applications: A review, Building and Environment 206 (2021) 108315. doi:10.1016/j.buildenv.2021.108315.
- [50] L. Sun, H. Gao, S. Pan, J.-X. Wang, Surrogate modeling for fluid flows based on physics-constrained deep learning without simulation data, Computer Methods in Applied Mechanics and Engineering 361 (2020) 112732. doi:10.1016/j.cma.2019.112732.
- [51] R. Shi, Z. Mo, K. Huang, X. Di, Q. Du, A Physics-Informed Deep Learning Paradigm for Traffic State and Fundamental Diagram Estimation, IEEE Transactions on Intelligent Transportation Systems 23 (8) (2022) 11688–11698. doi:10.1109/TITS.2021.3106259.
- [52] T. Xie, J. C. Grossman, Crystal Graph Convolutional Neural Networks for an Accurate and Interpretable Prediction of Material Properties, Physical Review Letters 120 (14) (2018) 145301, publisher: American Physical Society. doi:10.1103/PhysRevLett.120.145301.
- [53] J. B. Maguire, D. Grattarola, V. K. Mulligan, E. Klyshko, H. Melo, XENet: Using a new graph convolution to accelerate the timeline for protein design on quantum computers, PLOS Computational Biology 17 (9) (2021) e1009037, publisher: Public Library of Science. doi:10.1371/journal.pcbi.1009037.